

# Correlation Between Sn Grain Orientation and Corrosion in Sn-Ag-Cu Solder Interconnects

TAE-KYU LEE,<sup>1,3</sup> BO LIU,<sup>1</sup> BITE ZHOU,<sup>2</sup> THOMAS BIELER,<sup>2</sup>  
and KUO-CHUAN LIU<sup>1</sup>

1.—Component Quality and Technology Group, Cisco Systems, Inc., San Jose, CA 95134, USA.  
2.—Chemical Engineering and Materials Science, Michigan State University, East Lansing, MI 48824-1226, USA. 3.—e-mail: taeklee@cisco.com

The impact of a marine environment on Sn-Ag-Cu interconnect reliability is examined using salt spray exposure followed by thermal cycling. Sn-Ag-Cu solder alloy wafer-level packages, with and without pretreatment with 5% NaCl salt spray, were thermally cycled to failure. The prior salt spray reduced the characteristic lifetime of the Sn-Ag-Cu solder joints by over 43%. Although Sn-based materials show strong resistance to corrosion, the nature of localized corroded areas at critical locations in the solder joint caused significant degradation in the Sn-Ag-Cu solder joints. An important link between the corrosion path and Sn grain orientation was observed using orientation imaging microscopy (OIM). A strong correlation between the corrosion path and grain orientation was identified, indicating that the corrosion attack preferentially followed the basal plane of the Sn lattice.

**Key words:** Pb-free solder, Sn grain orientation, salt spray, corrosion, orientation image microscopy (OIM), thermal fatigue

## INTRODUCTION

Pb-free solder has not been in use in the field for long, and the amount of data concerning the corrosion properties of Pb-free products is limited. Thus, it is critical to investigate the sensitivity of Pb-free solder joint reliability in various environmental conditions to evaluate the field performance of Pb-free products, and it is also crucial to investigate the corrosion mechanism and its dependency on microstructure in solder joint interconnects. Telecommunication equipment is increasingly placed on seashores, cruise ships, and marine rescue vehicles. In these environments the equipment is continuously exposed to salt water or vapor even in enclosed casings. Due to the high reliability requirement and long lifetime expectations, the influence of salt water and vapor on the reliability of products in those environments needs to be quantified. It has been shown that corrosion-related

phenomena depend not only on the material property itself but also on cross-functional phenomena with the base microstructure.<sup>1-4</sup> Even though the results of various studies show that Sn-3.0Ag-0.5Cu (wt.%) (SAC305) solder exhibits better corrosion resistance than other Sn-based alloy compositions (including Sn-Pb) due to its high noble-metal content (Ag and Cu) and its theoretically stable structure,<sup>6-9</sup> the combination of localized corrosion and thermal cycling stress concentrations can degrade the material, which must be considered for certain environmental applications. However, a recent study on the thermal fatigue performance of Sn-Pb and Sn-Ag-Cu solder alloys showed that the dual-phase microstructure of Sn-Pb is relatively resistant to corrosion, but the more stable Sn-Ag-Cu showed deeper degradation due to corrosion penetration at critical locations.<sup>1,5</sup>

The main component of Pb-free solder alloys, tin (Sn), resists corrosion because of the passivity of the film that forms on its surface.<sup>6,7,10</sup> The Ag and Sn in SAC305 solder react with each other to form an intermetallic compound (IMC) (Ag<sub>3</sub>Sn), which is evenly distributed in the matrix. The Cu and Sn in

(Received October 8, 2010; accepted April 15, 2011;  
published online May 20, 2011)

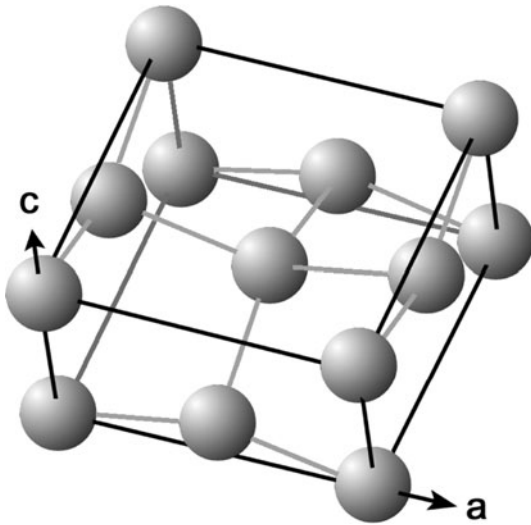


Fig. 1.  $\beta$ -Sn crystal structure.

SAC305 solder are known to form the intermetallic compound  $(\text{Cu,Ni})_6\text{Sn}_5$  or  $\text{Cu}_6\text{Sn}_5$ , depending on the package surface finish, at the interface of the solder and inside the solder bulk. Because these IMCs are chemically stable, they are nearly insoluble in etchants, making them stable against corrosion. While these intermetallic precipitates may function as noble materials, they can also facilitate reactions with the Sn by forming galvanic couples.<sup>11</sup>

In addition to the role of IMCs as galvanic couples in solder joints, the impact of the Sn grain orientation needs further investigation as well. Lead-free solder alloys have strong anisotropic thermal expansion and plastic deformation characteristics, resulting in mechanical properties that differ significantly from Sn-Pb joints.<sup>12–15</sup> Compared with Sn-Pb solder joints, each individual lead-free solder joint has its own unique characteristics arising from its anisotropic tetragonal Sn lattice. Because Pb-free solder alloys consist of more than 95% (wt.%) Sn, the mechanical and thermal behavior is dominated by the Sn microstructure. As shown in Fig. 1, Sn has a body-centered tetragonal (bct) structure with additional atoms located at lattice positions  $(0.5, 0, 0.25)$  and  $(0, 0.5, 0.75)$ .<sup>16</sup> These extra atoms form a tetrahedral bonding arrangement with the body-center atom, similar to that observed in the diamond cubic crystal structure.<sup>17</sup> Because  $\beta$ -Sn is stiffest in the direction in which it expands the most, substantial internal stresses develop in polycrystals, causing heterogeneous deformation near grain boundaries during thermal cycling.<sup>18</sup> Recent studies of the nature of Sn revealed new information and showed important consequences of the large-grain nature of Pb-free solder joints.<sup>18–20</sup> Though many recent research efforts have sought to understand the deformation mechanisms of solder joints,<sup>21–28</sup> few publications have considered the effect of Sn grain orientation on corrosion.

In this study, the thermal fatigue reliability of SAC305 solder joints was investigated under the influence of prior exposure to a harsh marine environment. Locally corroded areas were observed, followed by testing to determine whether the corroded regions accelerate crack initiation or propagation, thereby posing a risk to the long-term reliability of the solder joint. The reason for the thermal cycling was to identify the magnitude of degradation associated with prior corrosion caused by salt water or vapor. Thermal cycling tests were conducted in accelerated tests to assess the lifetime of the interconnect or solder joints under function. The initial corrosion observations suggested that crack initiation may be accelerated, but accelerated thermal cycling tests were conducted to assess the impact of salt on thermal fatigue damage evolution. Given the fact that corrosion occurs in small areas, a package type with a relatively small solder ball size that experiences a high degree of stress during thermal cycling was selected, i.e., the wafer-level chip-scale package (WLCSPP). The microstructures were analyzed using orientation image microscopy (OIM™) to observe the correlation between the Sn grain orientation and the corrosion path, and to identify microstructural evolution as well as possible mechanisms that affect, and the extent of, degradation of solder joints caused by corrosion.

## EXPERIMENTAL PROCEDURES

The WLCSPP packages 7 mm  $\times$  6 mm in body size used in this study had a solder ball pitch of 0.5 mm (i.e., the distance from one solder ball to the adjacent one) and a 10  $\times$  10 full array matrix (less two solder joints, total of 98 joints) of Sn-3.0Ag-0.5Cu (wt.%) (SAC305) solder balls, which were 250  $\mu\text{m}$  in diameter, as shown in Fig. 2. The package-side metallurgy had an electrolytic NiAu surface finish, and the parts were board-assembled on 2.4 mm thick, high glass transition temperature ( $T_g$ ), FR4 printed circuit boards that had Cu pads with organic surface preservative (OSP) surface finish. Sn-3.0Ag-0.5Cu (wt.%) (SAC305) solder paste was used for the SAC305 solder ball parts with a typical peak temperature of 240°C and 60 s above the liquidus temperature in the reflow profile. The salt spray test was conducted according to the ASTM B117-09 protocol,<sup>29</sup> i.e., the test specimens were exposed to 5% (wt.%) sodium chloride (NaCl) aqueous solution (or fog) at 35°C for 96 h in an enclosed chamber. After the salt spray test, salt deposits were removed by a gentle rinse of deionized water at room temperature, followed by drying in a dry chamber. Thermal cycling tests were performed on samples with and without this prior exposure to salt; samples were tested with a 0°C to 100°C thermal cycle at a ramp rate of 10°C/min with a 10 min dwell time. Continuous resistivity measurement was applied for in situ monitoring during the test. The failure criterion in this study was

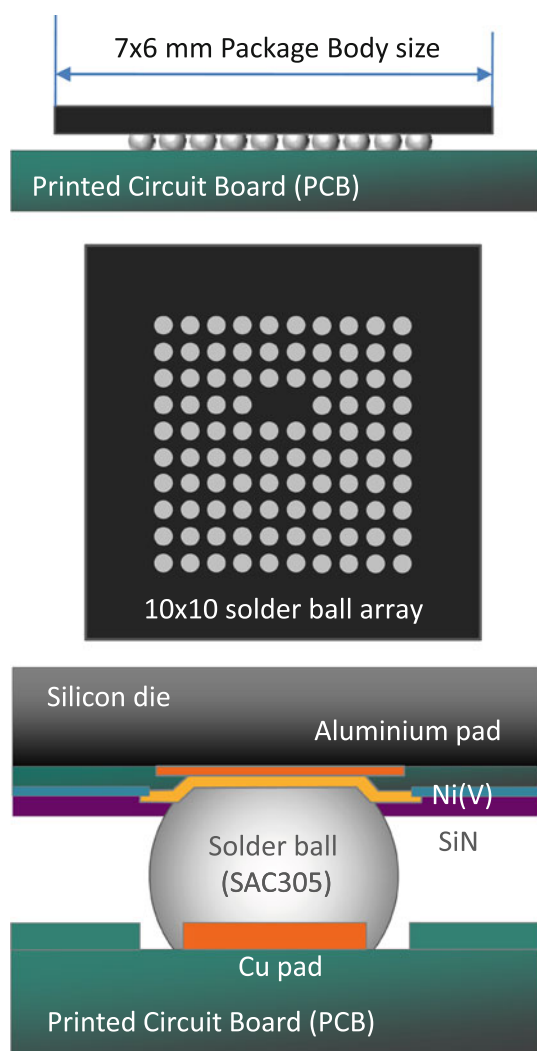


Fig. 2. Schematic drawing of a wafer-level chip-scale package (WLCSP) sample.

a 20% increase of peak resistivity compared with the initial value. A total of 32 components per condition were tested, and the results were plotted on Weibull distribution plots. The failed samples were subjected to cross-sectional analysis to compare the evolution of the microstructures with non-salt-exposed samples, and to identify the locations and morphology of the solder joint cracks. For Sn grain orientation analysis, selected joints were imaged using both polarized light microscopy and OIM with a high-resolution step size. Carbon paint was used to cover the surrounding epoxy mounting material to enable good image quality using a Link/TSL OIM™ system installed on a CamScan 44FE electron microscope.<sup>16,19,30</sup>

## RESULTS AND DISCUSSION

Figure 3 shows the initial microstructure following board assembly. Both package-side and board-side interfaces have near scallop-type intermetallic

morphology, identified as  $(\text{Cu,Ni})_6\text{Sn}_5$ . A fine  $\text{Ag}_3\text{Sn}$  precipitate network can be observed inside the Sn base matrix of the solder joint.

The Weibull plot shown in Fig. 4 shows the thermal cycling results for samples with and without pretreatment in a 5% NaCl aqueous environment for 96 h. The characteristic number of thermal cycles, which is the cycle number for 63.5% failure rate, was 1384 cycles for as-assembled and non-salt spray treated components, but it was reduced to 786 cycles for the components treated by the salt spray, which is a 43% reduction in characteristic lifetime.

Figure 5 shows cross-sections of an edge row (joints A1 to A10) from a sample from each group which failed near the characteristic life cycle number. Figure 5a shows the sample thermally cycled to failure without any pretreatment. The fatigue crack initiated and propagated along the package-side interface inside the bulk solder. Full cracks are observed in many joints, particularly those on the left side. Partially cracked solder joints are also observed in the middle of the package and the rightmost joint. In contrast, Fig. 5b shows a cross-section from a sample treated in 5% NaCl salt spray for 96 h and then thermally cycled to failure. Compared with the cross-section images in Fig. 5a, numerous corrosion regions can be observed; for example, joints A1 and A2 in Fig. 5b show a  $\sim 45^\circ$  angle corrosion trace penetrating from the upper region of the solder joint inward to the bulk solder, whereas joints A3 and A5 show horizontal penetration. These localized corrosion areas at the corners of the solder joints probably degraded the thermal cycling performance of the solder joints and reduced the characteristic lifetime as shown in Fig. 4.

Along with the characteristic lifetime reduction from NaCl pretreatment, the corrosion path and penetration directions are important for understanding the degradation mechanism. As shown in joints A1 to A5 in Fig. 5b, the corrosion paths had differing orientations, possibly due to Sn grain orientation, so OIM analysis was conducted to assess this possibility. Figure 5c, d shows orientation maps corresponding to the SEM image of each joint, revealing joints with single- and multicrystal orientations. Each color represents a different  $c$ -axis orientation with respect to the substrate and package (Table I). “Red-oriented” joints have the  $c$ -axis nearly parallel to the substrate plane. In “blue-oriented” joints the  $c$ -axis is highly inclined to the package plane.<sup>16</sup> While the rightmost joint in Fig. 5a is at a corner site, its blue orientation resisted cracking more effectively than the red orientations on the left side.

The correlation between the Sn grain orientation and corrosion path can be seen in Fig. 5d. Joints A2, A5, and A10 are shown in greater detail in Fig. 6. The SEM image of joint A2 shows corroded regions at the package-side interface corners, and,

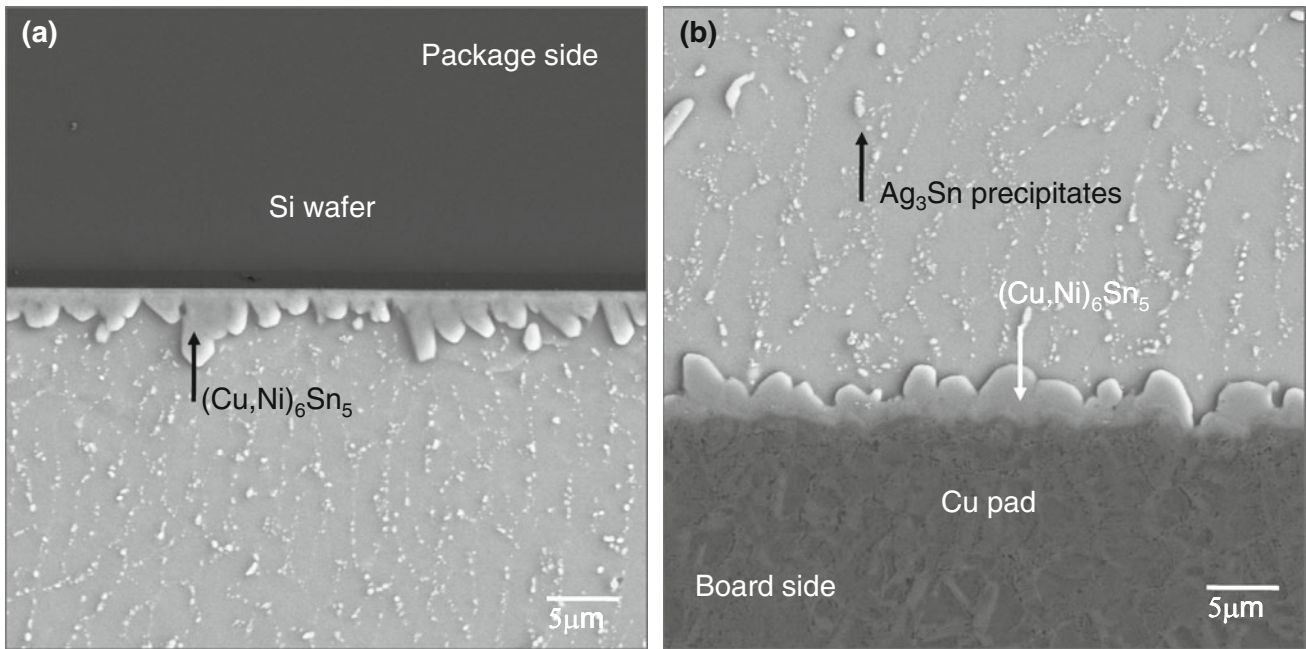


Fig. 3. Cross-section SEM image of as-assembled WLCSP package microstructure: (a) SAC305 solder joint package-side interface and (b) board-side interface.

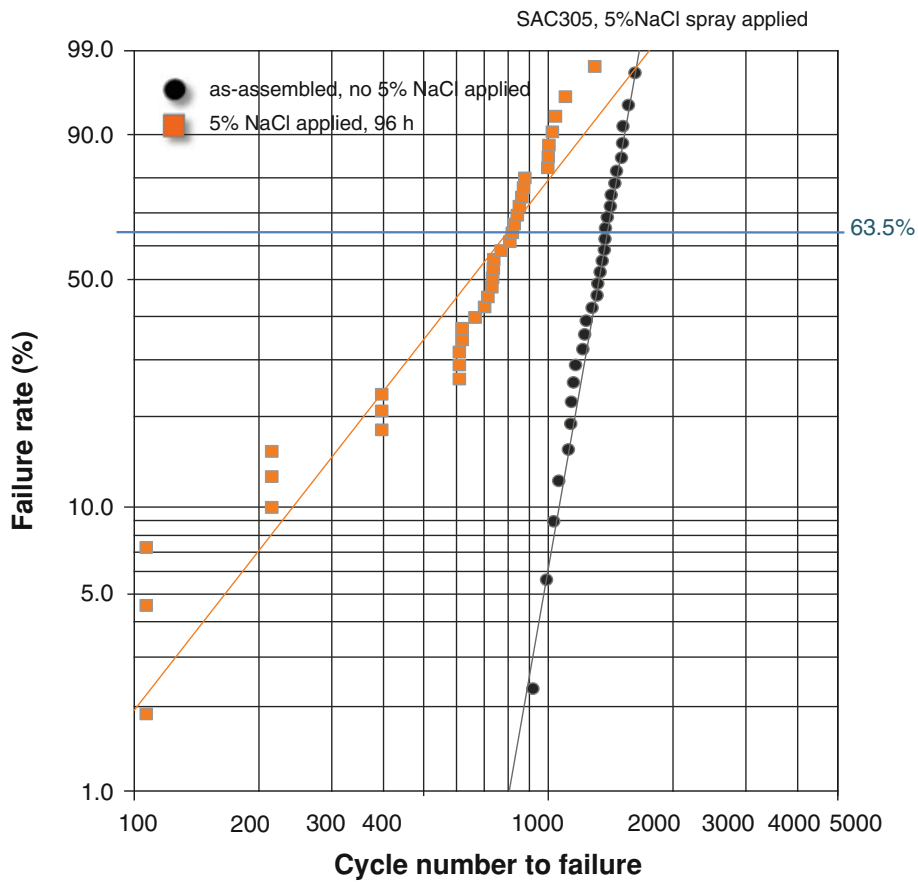


Fig. 4. Weibull plot for the thermal cycling results with and without prior 5% NaCl salt spray preconditioning.

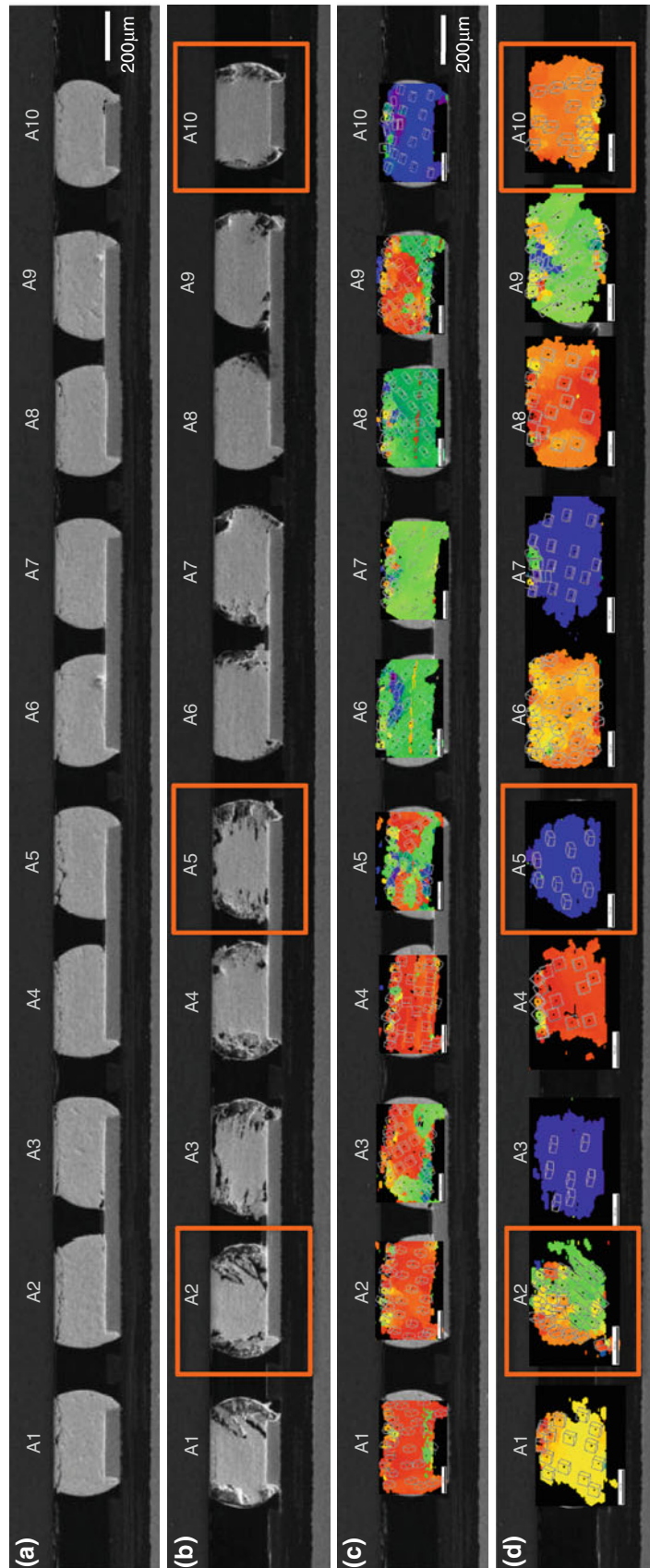



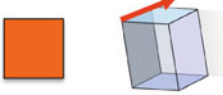

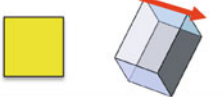

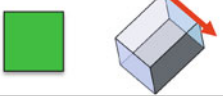





Fig. 5. Cross-section SEM image of thermally cycled edge row (joints A1 to A10) of the WL CSP assembled package (a, c), and for a different package preconditioned with 5% NaCl prior to thermal cycling (b, d). The c-axis orientation maps for the joints shown in (a, b) are presented in (c, d), respectively.

**Table I. Sn grain orientation color code used with OIM to identify the *c*-axis inclination from the interface**

Category		
Color code with lattice structure based on <i>c</i> -axis orientation Each OIM images have the color Code and the lattice associated with it.		Cross section side view orientation Each color code shows the <i>c</i> -axis orientation
Red		
Orange		
Yellow		
Green		
Blue/Purple		

as indicated by white arrows, the corrosion paths had a distinguishable direction, which points downwards with an angle that differs on either side. The same joint with the OIM image overlapped is shown in Fig. 6b, which allows comparison of the Sn grain orientation with the crack direction. The corrosion path aligns with the Sn lattice basal plane and penetrates along the Sn grain basal plane into the bulk solder joint; the angle of the basal plane differs on either side of the joint, due to different crystal orientations. While this joint is severely corroded, it did not crack. Figure 6c and d show the SEM and overlapping OIM image for joint A5. The Sn grain *c*-axis is perpendicular to the package side and shows a single-crystal, blue-oriented grain orientation, in which the basal plane is aligned parallel to the package-side interface. The corrosion path shown in Fig. 6c also matches the basal plane direction, and a continuous crack is visible near the top of the joint. In contrast to the blue-oriented solder joints in Fig. 6c, d, Fig. 6f shows a *c*-axis direction parallel to the package interface and thus the basal plane is perpendicular to the interface. This crystal orientation allowed corrosion to occur from the edges of the joint inward, particularly at the corners of the solder joint, either from the package-side corners or from the board-side interface corners. Due to this orientation, the corrosion attack occurred fairly uniformly along the edges of the solder ball,

with no deep penetration into the joint, but the joint developed a crack on the package side of the joint.

The observations shown here provide the opportunity to identify a mechanism that could not be identified without knowing the Sn grain orientation, allowing a correlation between corrosion and crystal orientation to be identified. First, there is a correlation between the Sn lattice basal plane and the preferential corrosion path. Second, this study reveals the potential susceptibility of blue-oriented solder joints to corrosion attack. As shown in Fig. 6c, d, blue-oriented joints, in which the basal planes are aligned nearly parallel to the package-side interface, have more corrosion attack points. The corners of the solder joint on the package-side interface are sites with greater potential for fatigue cracks due to the stress concentration during thermal cycling, thus solder joints with corrosion in blue-oriented joints are at potentially higher risk of earlier crack initiation and crack propagation than in joints with other orientations, because the corrosion penetration is inward along the interface. This observation is somewhat unexpected because, based upon a purely thermal cycling performance point of view, the blue-oriented joints are the most resistant to thermal fatigue due to this *c*-axis orientation, as shown in other studies.<sup>16</sup> However, when corrosion is considered as an important factor, the blue-oriented joints are among the worst performers in thermal cycling. Compared with these blue-oriented joints, the orange-oriented joint in Fig. 6f shows a lesser amount of attack, yet it still cracked, probably due to the vulnerability of this orientation to tensile fracture in the hot part of the thermal cycle.<sup>17</sup> Even if this joint is corroded at the corner of the joint, because the corrosion follows the basal plane orientation, the corrosion does not morphologically generate a crack shape into the interior of the joint, instead causing blunt degradation along the surface. While degradation can be expected, the impact on thermal cycling will be less than that of the blue-oriented joint shown in Fig. 6c, d.

## CONCLUSIONS

This work focused on the long-term reliability of Sn-Ag-Cu solder joint interconnects in environments containing sodium chloride (e.g., marine). WLCSPs with and without pretreatment by a 5% NaCl salt spray environment for 96 h were thermally cycled to failure. This series of tests revealed a characteristic lifetime reduction of over 43%. Although Sn-based materials show strong resistance to corrosion, the localized nature of the corroded areas at critical locations in the solder joint caused significant degradation of thermal fatigue performance in Sn-Ag-Cu solder joints. An important link between the corrosion path and Sn lattice basal plane was observed using orientation image

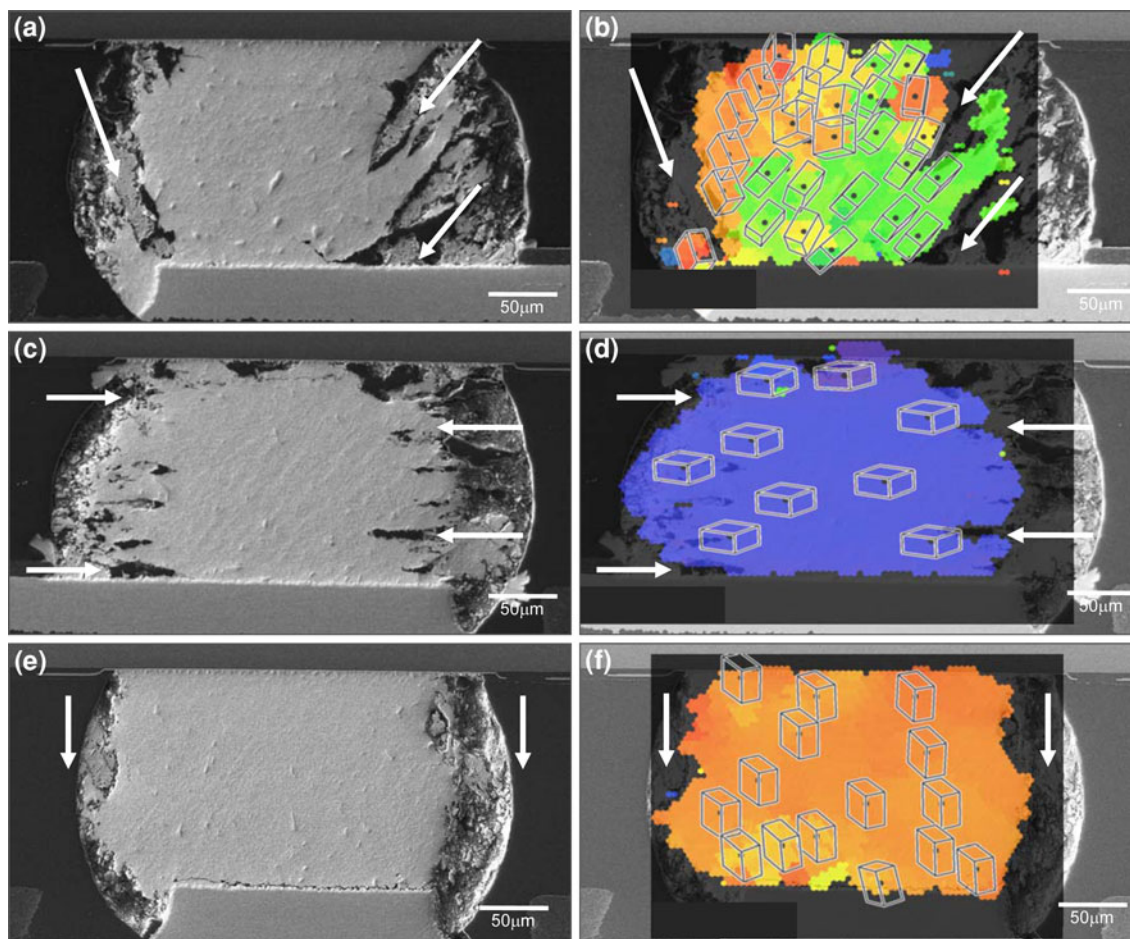


Fig. 6. Enlarged SEM images and OIM maps for 5% NaCl preconditioned joints A2 (a, b), A5 (c, d), and A10 (e, f), showing how the corrosion attack is correlated with the Sn lattice basal planes.

microscopy (OIM), indicating that joints that are resistant to thermal cycling (joints with the *c*-axis perpendicular to the substrate) are particularly susceptible to corrosive attack.

#### ACKNOWLEDGEMENTS

This work is a collaborative research project between the Cisco Component Quality and Technology Group and Michigan State University and is funded by Cisco Systems, Inc.

#### REFERENCES

1. F. Song and R. Lee, *Proceeding of the 56th Electronic Components and Technology Conference*, San Diego, California, May (2006).
2. M. Abtey and G. Selvaduray, *Mater. Sci. Eng. R* 27, 95 (2000).
3. A.J. Hale and H.S. Fosteh, *J. Soc. Chem. Ind.* 9, 2371 (1915).
4. A. Jermstad and A. Gaule, *J. Inst. Met.* 13, 1370 (1919).
5. B. Liu, T.-K. Lee, and K.-C. Liu, *42nd International Symposium on Microelectronics (IMAPS 2009) Proceedings*, San Jose, 3rd November (2009).
6. M. Mori, K. Miura, T. Sasaki, and T. Ohtsuka, *Corros. Sci.* 44, 887 (2002).
7. U.S. Mohanty and K. Lin, *Corros. Sci.* 50, 2437 (2008).
8. R.P. Frankenthal and D.J. Siconolfi, *Corros. Sci.* 21, 479 (1981).
9. T. Farrell, *Met. Sci.* 10, 87 (1976).
10. B.Y. Wu, Y.C. Chan, and M.O. Alam, *J. Mater. Res.* 21, 62 (2006).
11. J.Y. Jung, S.B. Lee, H.Y. Lee, Y.C. Joo, and Y.B. Park, *J. Electron. Mater.* 37, 1111 (2008).
12. D. Frear, H. Morgan, and J.H. Lau, eds., *The Mechanics of Solder Alloy Interconnects* (New York: Van Nostrand Reinhold, 1994).
13. J.A. Rayne and B.S. Chandrasekhar, *Phys. Rev.* 120, 1658 (1960).
14. D.G. House and E.V. Vernon, *Br. J. Appl. Phys.* 11, 254 (1960).
15. V.T. Deshpande and D.B. Sirdeshmukh, *Acta Cryst.* 15, 294 (1962).
16. T.-K. Lee, B. Zhou, L. Blair, K.-C. Liu, and T.R. Bieler, *J. Electron. Mater.* 39, 2588 (2010).
17. T.R. Bieler, H. Jiang, L.P. Lehman, T. Kirkpatrick, E.J. Cotts, and B. Nandagopal, *IEEE Trans. Compon. Packag. Technol.* 31, 370 (2008).
18. A.U. Telang, T.R. Bieler, J.P. Lucas, K.N. Subramanian, L.P. Lehman, Y. Xing, and E.J. Cotts, *J. Electron. Mater.* 33, 1412 (2004).
19. B. Zhou, T.R. Bieler, T.-K. Lee, and K.-C. Liu, *J. Electron. Mater.* 38, 2702 (2009).
20. T.-K. Lee, K.-C. Liu, and T.R. Bieler, *J. Electron. Mater.* 38, 2685 (2009).

21. S. Park, R. Dhakal, L. Lehman, and E. Cotts, *Acta Mater.* 55, 3253 (2007).
22. S. Terashima, T. Kobayashi, and M. Tanaka, *Sci. Technol. Weld. Join.* 13, 732 (2008).
23. M.A. Matin, E.W.C. Coenen, W.P. Vellinga, and M.G.D. Geers, *Scripta Mater.* 53, 927 (2005).
24. A.U. Telang and T.R. Bieler, *Scripta Mater.* 52, 1027 (2005).
25. A.U. Telang, T.R. Bieler, A. Zamiri, and F. Pourboghra, *Acta Mater.* 55, 2265 (2007).
26. M.A. Matin, W.P. Vellinga, and M.G.D. Geers, *Mater. Sci. Eng. A* 445, 73 (2007).
27. A. LaLonde, D. Emelander, J. Jeannette, C. Larson, W. Rietz, D. Swenson, and D.W. Henderson, *J. Electron. Mater.* 33, 1545 (2004).
28. T.R. Bieler, T.-K. Lee, and K.-C. Liu, *J. Electron. Mater.* 38, 2712 (2009).
29. ASTM B117-09, *Standard Practice for Operating Salt Spray (Fog) Apparatus* (2009).
30. B. Zhou, T.R. Bieler, G. Wu, S. Zaefferer, T.-K. Lee, and K.-C. Liu, *42nd International Symposium on Microelectronics (IMAPS 2009) Proceedings*, San Jose, 3rd November (2009).